

# Thermal study on electrospun polyvinylpyrrolidone/ammonium metatungstate nanofibers: optimising the annealing conditions for obtaining $\text{WO}_3$ nanofibers

Imre Miklós Szilágyi · Eero Santala · Mikko Heikkilä ·  
Marianna Kemell · Timur Nikitin · Leonid Khriachtchev ·  
Markku Räsänen · Mikko Ritala · Markku Leskelä

Niimistö's Special Chapter  
© Akadémiai Kiadó, Budapest, Hungary 2011

**Abstract** This article demonstrates how important it is to find the optimal heating conditions when electrospun organic/inorganic composite fibers are annealed to get ceramic nanofibers in appropriate quality (crystal structure, composition, and morphology) and to avoid their disintegration. Polyvinylpyrrolidone [PVP,  $(\text{C}_6\text{H}_9\text{NO})_n$ ] and ammonium metatungstate [AMT,  $(\text{NH}_4)_6[\text{H}_2\text{W}_{12}\text{O}_{40}] \cdot n\text{H}_2\text{O}$ ] nanofibers were prepared by electrospinning aqueous solutions of PVP and AMT. The as-spun fibers and their annealing were characterized by TG/DTA-MS, XRD, SEM, Raman, and FTIR measurements. The 400–600 nm thick and tens of micrometer long PVP/AMT fibers decomposed thermally in air in four steps, and pure monoclinic  $\text{WO}_3$  nanofibers formed between 500 and 600 °C. When a too high heating rate and heating temperature ( $10\text{ }^{\circ}\text{C min}^{-1}$ , 600 °C) were used, the  $\text{WO}_3$  nanofibers completely disintegrated. At lower heating rate but too high temperature ( $1\text{ }^{\circ}\text{C min}^{-1}$ , 600 °C), the fibers broke into rods. If the heating rate was adequate, but the annealing temperature was too low ( $1\text{ }^{\circ}\text{C min}^{-1}$ , 500 °C), the nanofiber morphology was excellent, but the sample was less crystalline. When the

optimal heating rate and temperature ( $1\text{ }^{\circ}\text{C min}^{-1}$ , 550 °C) were applied,  $\text{WO}_3$  nanofibers with excellent morphology (250 nm thick and tens of micrometer long nanofibers, which consisted of 20–80 nm particles) and crystallinity (monoclinic  $\text{WO}_3$ ) were obtained. The FTIR and Raman measurements confirmed that with these heating parameters the organic matter was effectively removed from the nanofibers and monoclinic  $\text{WO}_3$  was present in a highly crystalline and ordered form.

**Keywords**  $\text{WO}_3$  · PVP · Annealing · TG/DTA-MS · XRD · SEM · Raman · FTIR

## Introduction

One-dimensional (1D) nanomaterials, such as nanowires, nanofibers, nanorods, nanowhiskers, nanobelts, nanoribbons, and nanotubes have attracted great attention in recent years. They have already demonstrated outstanding electrical, magnetic, acoustic, optical, mechanical, thermal, sensing, and catalytic properties [1–4]. Various vapor phase (e.g., vapor–liquid–solid synthesis [5], laser ablation [6]), solution phase (e.g., hydrothermal, solvothermal, solution–liquid–solid syntheses [7]), and template directed (e.g., electrochemical anodization–reanodization and etching [8], atomic layer deposition [9]) techniques have been developed to obtain these materials.

Electrospinning is a recent method of choice to prepare 1D nanostructures. It offers a simple and convenient way for making polymer, inorganic, and composite fibers with both solid and hollow interiors. The produced fibers are usually extremely long (up to several hundreds of micrometers) and have uniform diameters ranging between tens of nanometers to several micrometers [10–13]. In

I. M. Szilágyi · E. Santala · M. Heikkilä · M. Kemell ·  
T. Nikitin · L. Khriachtchev · M. Räsänen · M. Ritala ·  
M. Leskelä

Department of Chemistry, University of Helsinki,  
P.O. Box 55, 00014 Helsinki, Finland

I. M. Szilágyi (✉)  
Materials Structure and Modeling Research Group  
of the Hungarian Academy of Sciences, Department of Inorganic  
and Analytical Chemistry, Budapest University of Technology  
and Economics, Szt. Gellért tér. 4, 1111 Budapest, Hungary  
e-mail: imre.szilagyi@mail.bme.hu

electrospinning, a high static voltage is applied to a polymer or polymer/inorganic solution. Under the strong electrostatic force, the solution is ejected from a nozzle. The charged jet is accelerated by the electric field, dries, and is deposited in the form of nanofibers onto a grounded substrate [14, 15].

When inorganic nanofibers are the target of electrospinning, the as-spun polymeric/inorganic composite fibers are calcined to remove the organic material. Proper calcination is a key step in obtaining high-quality inorganic nanofibers, as they are very brittle and can easily disintegrate to nanoparticles. Up to now, in annealings of electrospun fibers quite many different heating programs have been used, i.e., the heating temperature (300–1000 °C), the heating rate (0.5–5 °C min<sup>-1</sup>), and the dwell time at the set temperature (1–12 h) varied in wide ranges [2, 10–21]. This shows that it is vital to find the appropriate annealing parameters for each polymer/inorganic composite. The annealing parameters depend mostly on the decomposition temperature of the polymer, the formation temperature of the targeted inorganic crystalline phase, and the mechanical stability of the inorganic nanofibers.

Though proper calcination is vital in getting high-quality electrospun ceramic nanofibers, only few studies have mentioned its importance [11, 13, 17]. Up to now, to the best of our knowledge, only TG and TG/DTA curves of electrospun polymer/inorganic nanofibers have been published [2, 11, 12, 14, 18–20], but these are not detailed thermoanalytical studies, and none of them used evolved gas analysis.

Here we present a model study on the heat treatment of electrospun polyvinylpyrrolidone [PVP, (C<sub>6</sub>H<sub>9</sub>NO)<sub>n</sub>] and ammonium metatungstate [AMT, (NH<sub>4</sub>)<sub>6</sub>[H<sub>2</sub>W<sub>12</sub>O<sub>40</sub>]<sub>n</sub>H<sub>2</sub>O] nanofibers. It clearly demonstrates the importance of finding the appropriate annealing conditions for polymer/inorganic nanofibers prepared by electrospinning. We use the PVP/AMT fibers as a model system, as we have recently developed a new electrospinning process for preparing WO<sub>3</sub> nanofibers (detailed results about the process will be published elsewhere). This process is unique because it is completely water-based, thus environmentally friendly and easy to handle, in contrast to the few previous reported WO<sub>3</sub> electrospinning methods, which used organic solvents to dissolve the polymer and the inorganic precursors [15–17]. As discussed previously, it was necessary to optimize the heating program of the as-spun PVP/AMT nanofibers.

In this study, the PVP/AMT nanofibers are prepared by electrospinning aqueous solutions of PVP and AMT. The annealing process of the PVP/AMT fibers and the product WO<sub>3</sub> nanofibers are characterized by thermal analysis (TG/DTA) and evolved gas analysis with a mass spectrometer

(TG/DTA-MS), X-ray diffraction (XRD), scanning electron microscopy (SEM), FTIR, and Raman spectroscopy.

## Experimental section

The AMT/PVP nanofibers were prepared by electrospinning a 1:4 mixture of aqueous solutions of PVP [(C<sub>6</sub>H<sub>9</sub>NO)<sub>n</sub>, 20 wt%] and AMT ((NH<sub>4</sub>)<sub>6</sub>[H<sub>2</sub>W<sub>12</sub>O<sub>40</sub>]<sub>n</sub>H<sub>2</sub>O, 50 wt%). AMT (Fluka, 99% purity) and PVP (Alfa Aesar, *M*<sub>w</sub>: 1300,000) were used as received. The needle voltage was 14.4 kV. The polymer fibers were collected on a rotating drum 15 cm from the needle.

The thermal decomposition of the nanofibers was studied by a TG/DTA-MS apparatus consisting of an STD 2960 simultaneous TG/DTA (TA Instruments Inc.) thermal analyzer and a Thermostar GSD 200 (Balzers Instruments) quadrupole mass spectrometer. During the measurement, an open platinum crucible, sample size of 4.5 mg and heating rate of 10 °C min<sup>-1</sup> were used, and the thermoanalytical furnace was purged with flowing air (130 mL min<sup>-1</sup>). On-line coupling of the two parts (TG/DTA and MS) was provided through a heated (*T* = 200 °C) 100% trimethylsilyl deactivated fused silica capillary tube with an inner diameter of 0.15 mm. A mass range between *m/z* = 1–64 was monitored through 64 channels in multiple ion detection mode (MID) with a measuring time of 0.5 s/channel. The components of the released gas mixtures were monitored and identified on the basis of their MS reference gas spectra [22].

Annealing of the as-prepared PVP/AMT nanofibers was done in a Nabertherm N7 furnace equipped with a Logotherm S19 heating program controller. The fibers were heated with 10 or 1 °C min<sup>-1</sup> heating rate to 500, 550, or 600 °C (i.e., the heating period ranged between 48 min and 9.5 h), and the samples were kept at the set temperature for 1 h.

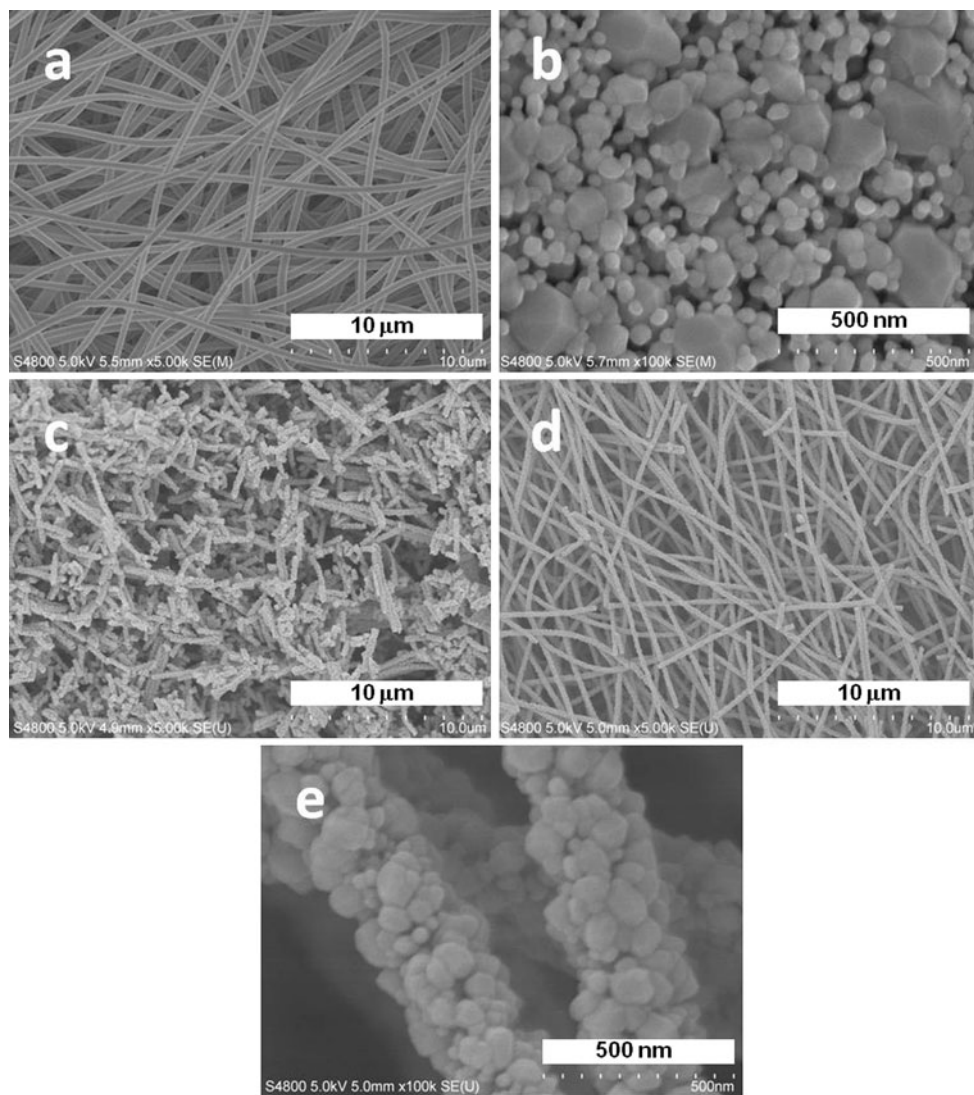
The XRD patterns were recorded by a PANalytical X'pert Pro MPD X-ray diffractometer using Cu K<sub>α</sub> radiation and grazing incidence angle mode.

The morphology of the nanofibers was investigated by a Hitachi S-4800 field emission scanning electron microscope (FESEM).

The FTIR measurements were conducted with a Bruker Vertex 80 FTIR spectrometer (liquid nitrogen cooled MCT detector, KBr beamsplitter and Globar light source). The spectral resolution was 2 cm<sup>-1</sup> and 100 scans were accumulated for one spectrum.

The Raman spectra were recorded with a LabRam HR confocal microscope (Horiba Jobin Yvon) using excitation at 488 nm of an Ar-ion laser (0.1–1 mW on sample), 100× objective and spectral resolution 2 cm<sup>-1</sup>.

**Fig. 1** **a** SEM images of electrospun PVP/AMT nanofibers, **b–e** SEM images of  $\text{WO}_3$  nanofibers obtained by annealing PVP/AMT nanofibers in air **b** at  $600\text{ }^\circ\text{C}$  using  $10\text{ }^\circ\text{C min}^{-1}$  heating rate and 4 h isothermal stage, **c** at  $600\text{ }^\circ\text{C}$  using  $1\text{ }^\circ\text{C min}^{-1}$  heating rate and 1 h isothermal stage, and **d, e** at  $550\text{ }^\circ\text{C}$  using  $1\text{ }^\circ\text{C min}^{-1}$  heating rate and 1 h isothermal stage



## Results and discussion

### Thermal decomposition and oxidation of PVP/AMT nanofibers

Electrospinning of the PVP/AMT polymer/inorganic solution was successful, and homogenous nanofibers were produced. The diameter of the PVP/AMT fibers was 400–600 nm, and the fibers were several tens of micrometers long (Fig. 1a).

We studied in detail the thermal behavior of the as-spun PVP/AMT nanofibers in air, so that we could determine the annealing temperature, where the organic part of the fibers decomposes and burns out completely. The TG/DTA curves of the thermal decomposition and combustion of PVP/AMT nanofibers in air are shown in Fig. 2, while the evolved gas analytical (EGA) curves of selected ions, recorded with the on-line coupled mass spectrometer, are

presented in Fig. 3. Note that the EGA curves show only qualitative information, and they are scaled so that all features can be seen.

The PVP/AMT decomposed and oxidized in four main steps. To explain the steps, the measured thermoanalytical curves were compared with previous data published about the thermal decomposition of PVP and AMT.

There is abundant information available about the thermal decomposition of PVP and PVP/inorganic composites, as they have applications in many areas (e.g., nanotechnology [23], materials science [24], fuel cells [25], pharmaceutical and biomedical applications [26–28], and cosmetics [29]). The decomposition of PVP and PVP/inorganic composites (including electrospun fibers) was studied previously both in air and  $\text{N}_2$ , and mostly TG [30–37] and TG/DTA studies were published [2, 10–12, 18–20, 38–44] and only one evolved gas analytical report exists [45].

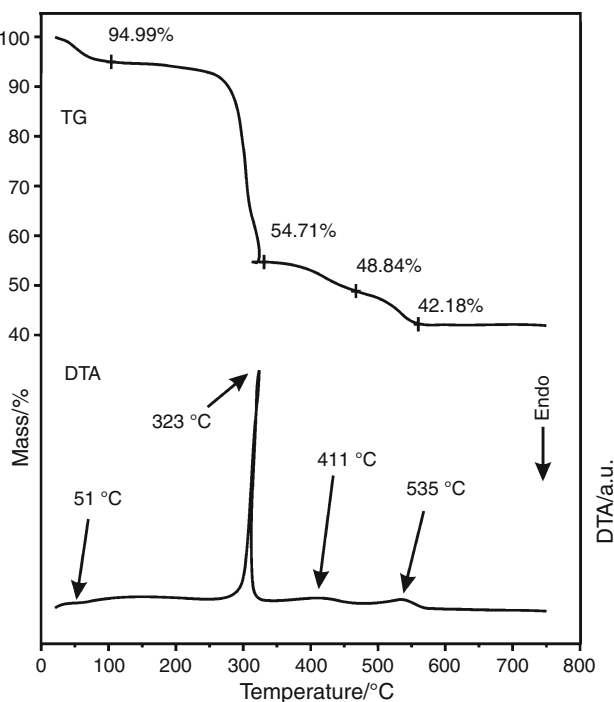


**Fig. 2** Simultaneous TG/DTA curves of PVP/AMT nanofibers measured in air ( $130 \text{ mL min}^{-1}$ ,  $10 \text{ }^{\circ}\text{C min}^{-1}$ , open Pt crucible, 4.5 mg)

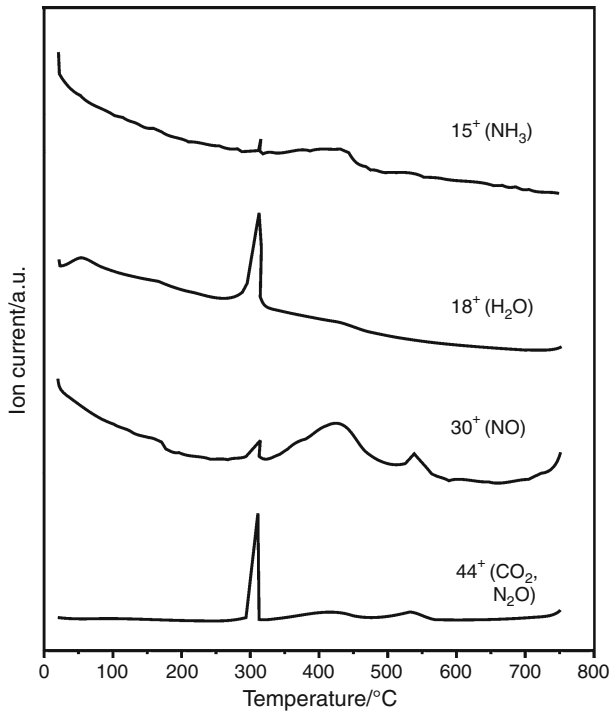


**Fig. 3** Evolved gas analytical (MS ion) curves of PVP/AMT nanofibers measured in air ( $130 \text{ mL min}^{-1}$ ,  $10 \text{ }^{\circ}\text{C min}^{-1}$ , open Pt crucible, 4.5 mg)

There are much less published data about the thermal behavior of AMT. To the best of our knowledge, no thermal study has been performed on pure AMT. However,

AMT was reported to be a decomposition intermediate of ammonium paratungstate (APT),  $(\text{NH}_4)_{10}[\text{H}_2\text{W}_{12}\text{O}_{42}] \cdot 4\text{H}_2\text{O}$  at  $200\text{--}250 \text{ }^{\circ}\text{C}$  [46, 47], though other studies could not confirm this [48]. The thermal behavior of APT is very well known as it is an important starting material for making tungsten oxides, tungsten carbides and tungsten metal for catalysis, hardmetals, and light source industry [49]. The thermal decomposition of APT has been characterized by various thermoanalytical (TG, DTA, and evolved gas analysis) and further techniques (e.g., XRD, SEM, FTIR, Raman, etc.) in oxidative, inert, and reductive atmospheres (see [48, 50–54] and the references therein). Thus, it was expected that the thermal decomposition of AMT should be similar to that of APT above  $200\text{--}250 \text{ }^{\circ}\text{C}$ .

Here in our study, at the first decomposition step ( $25\text{--}100 \text{ }^{\circ}\text{C}$ ) adsorbed water was released from both PVP and AMT (5% mass loss) in an endothermic reaction, shown by a small peak in the  $\text{H}_2\text{O}$  EGA curve ( $18^+$ ,  $\text{H}_2\text{O}^+$ ).

The second decomposition step took place between  $250$  and  $330 \text{ }^{\circ}\text{C}$ , where the largest mass loss occurred (40%). According to the previous thermal studies on PVP [2, 12, 18–20, 31, 37, 39, 44] in air, the main decomposition of PVP takes place in this temperature range. The dramatic weight loss in the TG curve was the result of the breakdown of the sidegroups (pyrrolidone) of PVP, which were released and oxidized immediately. The combustion of the evolved gaseous species was responsible for the sharp peaks in the  $\text{CO}_2$  ( $44^+$ ,  $\text{CO}_2^+$ ) and  $\text{H}_2\text{O}$  EGA curves, and it also explained the very sharp exothermic heat effect in the DTA curve, which occurred at  $323 \text{ }^{\circ}\text{C}$ . However, at this step not just PVP started to decompose, but also AMT. In the  $\text{NH}_3$  ( $15^+$ ,  $\text{NH}^+$ ) curve a small peak was observable, which suggested that part of the  $\text{NH}_4^+$  ions of AMT was released here.

At the third decomposition step ( $350\text{--}450 \text{ }^{\circ}\text{C}$ ), the main decomposition of AMT took place. This explanation was supported by that the largest peaks in the  $\text{NH}_3$  and  $\text{NO}$  ( $30^+$ ,  $\text{NO}^+$ ) EGA curves were observable in this region. Most probably  $\text{NH}_4^+$  ions and also  $\text{H}_2\text{O}$  molecules, which linked the large metatungstate ions, were released at this step (similar to the decomposition of APT), and in air they were burnt right away. In the case of the oxidation of APT [52],  $\text{NO}$  and  $\text{N}_2\text{O}$  ( $44^+$ ,  $\text{N}_2\text{O}^+$ ) were the main combustion products of as-released  $\text{NH}_3$  [55], and this was the case in the thermal oxidation of AMT as well. In parallel to the gas release, hexagonal (h-)  $\text{WO}_3$  or oxidized  $(\text{NH}_4)_x\text{WO}_3$  could form at  $460 \text{ }^{\circ}\text{C}$ , similarly to the case of annealing APT. It has recently been proven that h- $\text{WO}_3$  still contains small amount of impurities ( $\text{NH}_4^+$  or alkaline ions depending on the type of precursor), which stabilize its metastable structure [56]. Therefore,  $(\text{NH}_4)_x\text{WO}_3$  and h- $\text{WO}_3$  are

basically the same compounds [56, 57], the only difference between them is that the longitudinal hexagonal channels of  $(\text{NH}_4)_x\text{WO}_3$  are more packed with  $\text{NH}_4^+$  ions than that of h- $\text{WO}_3$ .

It is worth mentioning that the main decomposition of AMT happened at 50–80 °C higher temperature than expected, based on previous results on APT. In general, the main decomposition of the APT bulk takes place between 250 and 350 °C [48, 50–54], and an amorphous phase forms. From this, h- $\text{WO}_3$  or oxidized  $(\text{NH}_4)_x\text{WO}_3$  form in another decomposition step between 350 and 450 °C. In the case of AMT, these two stages could happen continuously in one step and at higher temperature than with APT, for which the presence of PVP might be responsible.

Based on previous results, the degradation of the residual hydrocarbon polymer chain of PVP also took place at the third step, but it could not be seen directly from the TG/DTA and EGA curves, as the decomposition of AMT was more intense, and the mass spectrometric signals of  $\text{N}_2\text{O}$  overlapped with  $\text{CO}_2$ . At the third decomposition stage, the combustion of  $\text{NH}_3$  and the organic material as well as the crystallization of  $(\text{NH}_4)_x\text{WO}_3$  and h- $\text{WO}_3$  [51, 52] resulted again in an exothermic DTA peak (411 °C), which was smaller than that at the second step.

At the last decomposition step (460–570 °C) the carbonized residue of PVP was burnt. In this final decomposition process, the as-formed h- $\text{WO}_3$  and  $(\text{NH}_4)_x\text{WO}_3$  could release their residual  $\text{NH}_4^+$  content, and transform into monoclinic (m-)  $\text{WO}_3$ . Again, a small exothermic peak was detected in the DTA curve in this region, the origin of which was the combustion of residual carbon and as-released  $\text{NH}_3$ , and also the exothermic hexagonal–monoclinic  $\text{WO}_3$  phase change [56].

The decomposition of the electrospun PVP/AMT nanofibers ended between 550 and 570 °C, and no further thermal processes were observed at higher temperatures up to 800 °C.

#### Optimizing the annealing conditions of PVP/AMT electrospun nanofibers

According to the TG/DTA-MS study, the organic content of the PVP/AMT nanofibers was burnt away completely by 550–570 °C. Therefore, it was straightforward to anneal the PVP/AMT fibers in a furnace at 600 °C, for which a 10 °C min<sup>-1</sup> heating rate (the same as at the TG/DTA-MS study) was used, and then the fibers were kept at 600 °C for 4 h. According to SEM images (Fig. 1b), the organic content was burnt completely and  $\text{WO}_3$  formed, but the  $\text{WO}_3$  nanofibers disintegrated, and only 50–250 nm  $\text{WO}_3$  particles were visible. This clearly demonstrated that a too high heating rate and too high annealing temperature might destroy the ceramic nanofibers, as was also mentioned and

shown in some previous electrospinning studies [11, 13, 17].

Therefore a much lower (1 °C min<sup>-1</sup>) heating rate was applied, and the PVP/AMT fibers were annealed at lower temperatures as well, i.e., at 550 and 500 °C and a shorter, 1 h long isothermal stage was used. At 600 °C and with a 1 °C min<sup>-1</sup> heating rate, the  $\text{WO}_3$  nanofibers did not disintegrate, but they still broke into 1–5 μm long and 250 nm wide nanorods, which were made up of 20–80 nm large particles (Fig. 1c). At 550 °C (Fig. 1d, e) and at 500 °C (not shown here), several ten micrometer long  $\text{WO}_3$  nanofibers were formed. These fibers were also 250 nm in diameter and were built up of 20–80 nm particles, just as those annealed at 600 °C. Larger 50–80 nm large particles were located at the surface of the fibers, while the inner part of the fibers was packed with smaller, 20–50 nm particles. The reason for such a size distribution of nanoparticles can be that higher mobility of particles at the surface of the fibers favors more intense grain growth.

The XRD patterns of the PVP/AMT fibers annealed at 500, 550, and 600 °C (1 °C min<sup>-1</sup> heating rate, 1 h isothermal stage) are shown in Fig. 4. All diffractograms correspond to pure, crystalline m- $\text{WO}_3$  (ICDD 43-1035 [58]). It is visible that as the annealing temperature rose, the XRD peaks got sharpened, i.e., the structure of m- $\text{WO}_3$  became more ordered. At 500 °C, the structure was considerably less crystalline than at 550 and 600 °C, and here the sample had a greenish-yellow color, suggesting an incompletely oxidized structure [56, 57]. The samples annealed at both 550 and 600 °C were yellow, thus fully

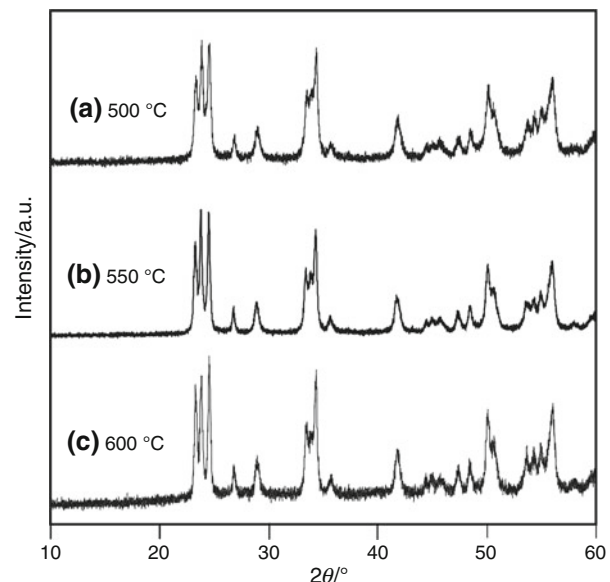


**Fig. 4** XRD patterns of  $\text{WO}_3$  nanofibers obtained by annealing PVP/AMT nanofibers using 1 °C min<sup>-1</sup> heating rate and 1 h isothermal stage in air at (a) 600 °C, (b) 550 °C, and (c) 500 °C

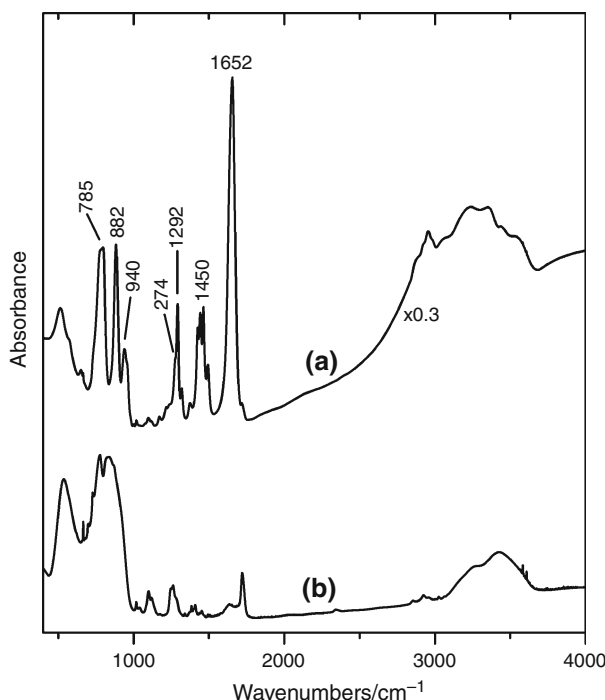


**Fig. 5** (a) IR spectrum of electrospun PVP/AMT nanofibers, (b) IR spectrum of  $\text{WO}_3$  nanofibers obtained by annealing PVP/AMT nanofibers in air at  $550\text{ }^\circ\text{C}$  using  $1\text{ }^\circ\text{C min}^{-1}$  heating rate and 1 h isothermal stage

oxidized, and the difference between their crystallinity was not quite significant.

As a fair compromise,  $550\text{ }^\circ\text{C}$  was selected for the annealing temperature of PVP/AMT nanofibers, and the heating rate was chosen to be  $1\text{ }^\circ\text{C min}^{-1}$ . Under these conditions the structure was as crystalline as possible, while the nanofiber arrangement of  $\text{WO}_3$  was still preserved.

Finally, to double-check the completeness of annealing (removal of organic species and formation of well-ordered structure of m- $\text{WO}_3$ ), the as-spun PVP/AMT fibers and the  $\text{WO}_3$  nanofibers prepared at  $550\text{ }^\circ\text{C}$  ( $1\text{ }^\circ\text{C min}^{-1}$  heating rate, 1 h isothermal stage) were also studied with FTIR and Raman spectroscopy.

The FTIR spectrum of PVP/AMT (Fig. 5a) was dominated by the bands of PVP [19, 26, 33, 35, 39]. The broad multiband region at  $3100\text{--}3450\text{ cm}^{-1}$  (3200, 3330, and  $3413\text{ cm}^{-1}$ ) was ascribed to the OH stretching vibrations of both PVP and AMT, while the band at  $3540\text{ cm}^{-1}$  could be explained by the NH stretching modes of AMT. The bands at  $2850\text{--}3000\text{ cm}^{-1}$  (2860, 2913, 2944, and  $2962\text{ cm}^{-1}$ ) were explained by the CH stretching vibrations of CH and  $\text{CH}_2$  in PVP. The most intense peak of PVP was the C=O stretching band at  $1652\text{ cm}^{-1}$ . Four IR modes at about  $1450\text{ cm}^{-1}$  (1422, 1440, 1462, and  $1473\text{ cm}^{-1}$ ) were due to the bending CH modes of  $\text{CH}_2$  of PVP and the

deformation mode of the  $\text{NH}_4^+$  ion [53] of AMT. The peak at  $1292\text{ cm}^{-1}$  and the shoulder at  $1274\text{ cm}^{-1}$  could be explained by the C–N and C–O stretching bands of PVP, respectively. The bands of AMT were observable mostly below  $1000\text{ cm}^{-1}$ . The W=O vibrations were detected at about  $940\text{ cm}^{-1}$  ( $930, 955\text{ cm}^{-1}$ ), and the W–O bands were visible at  $700\text{--}900\text{ cm}^{-1}$  ( $785, 882\text{ cm}^{-1}$ ). These bands were identified based on the FTIR data of polytungstates and  $\text{WO}_3$  [59–63], as the FTIR spectrum of AMT has not been published yet.

When the composite fibers were annealed at  $550\text{ }^\circ\text{C}$  (Fig. 5b), the PVP bands (e.g., at  $1652\text{ cm}^{-1}$ ) disappeared almost completely showing the effective removal of the organic material. Traces of organic fragments were suggested only by very weak bands at  $1652$  and  $2850\text{--}3000\text{ cm}^{-1}$ . However, the amount of these trace organics (in this study the absorbance of the peak at  $1652\text{ cm}^{-1}$  reduced 50 times from 3.13 to 0.06, when PVP/AMT was annealed at  $550\text{ }^\circ\text{C}$ ) was as low or even less than in other electrospinning studies [11, 18, 20, 21]. The broad peak between  $700$  and  $1000\text{ cm}^{-1}$  ( $723, 752, 805$ , and  $852\text{ cm}^{-1}$ ) in the FTIR spectrum of the sample annealed at  $550\text{ }^\circ\text{C}$  belonged to the W=O and W–O vibrations.

In the Raman spectrum of PVP/AMT (Fig. 6a), the bands of AMT were much more intense than the bands of PVP, which was in contrast to the FTIR results. Similar to

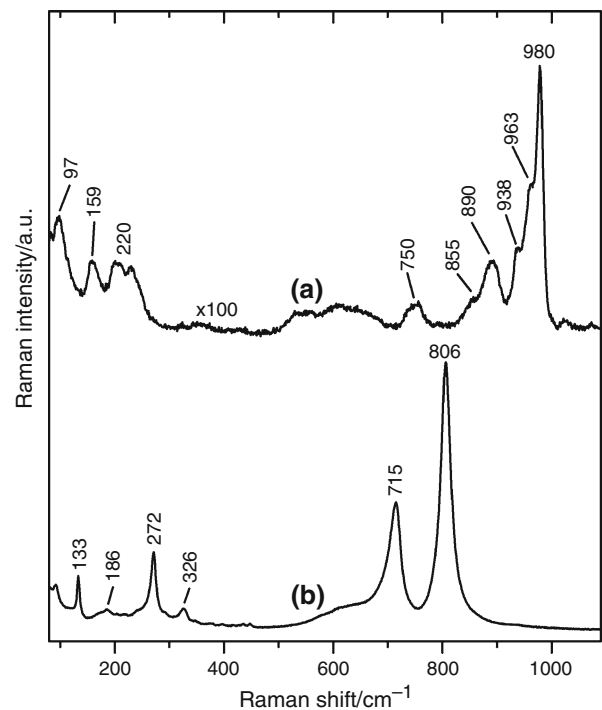


**Fig. 6** (a) Raman spectrum of electrospun PVP/AMT nanofibers, (b) Raman spectrum of  $\text{WO}_3$  nanofibers obtained by annealing PVP/AMT nanofibers in air at  $550\text{ }^\circ\text{C}$  using  $1\text{ }^\circ\text{C min}^{-1}$  heating rate and 1 h isothermal stage

the FTIR, the Raman spectrum of pure AMT has not been published yet, however, the supposed Raman bands of AMT could be identified based on the known Raman spectra of polytungstates [48, 61, 64–67]. The peak at  $980\text{ cm}^{-1}$  with shoulders at  $963$  and  $938\text{ cm}^{-1}$  ( $\text{W}=\text{O}$  bands) and the peak at  $890\text{ cm}^{-1}$  with a shoulder at  $855\text{ cm}^{-1}$  ( $\text{W}-\text{O}$  bands) are characteristic to polytungstates [48, 61, 64–67]. Similar to paratungstates [60, 64, 65], the weaker Raman peaks at  $500$ – $700\text{ cm}^{-1}$  ( $657$ ,  $618$ ,  $571$ ,  $540$ ,  $360$ , and  $337\text{ cm}^{-1}$ ) and about  $220\text{ cm}^{-1}$  ( $235$ ,  $210\text{ cm}^{-1}$ ) could also be assigned to AMT. One of the characteristic Raman peaks of PVP, the pyrrolidone ring breathing mode at  $934\text{ cm}^{-1}$  [13, 26–28, 40, 68], could not be observed, because the more intense Raman peaks of AMT between  $850$  and  $1000\text{ cm}^{-1}$  covered it completely. Similarly, the Raman peaks of PVP at  $858$  and  $556\text{ cm}^{-1}$  [26, 40, 68] were overlapped by the AMT bands. Nevertheless, the C–N vibration band at  $750\text{ cm}^{-1}$  [26, 27, 40, 68] clearly showed the presence of PVP, and some other Raman peaks of PVP could also be detected at  $371$ ,  $159$ , and  $97\text{ cm}^{-1}$  [40, 68].

When the PVP/AMT polymer was annealed at  $550\text{ }^{\circ}\text{C}$  (Fig. 6b), all the Raman bands of PVP disappeared, and only the Raman bands of pure m-WO<sub>3</sub> were present [58, 69–72]. The main bands at  $806$  and  $715\text{ cm}^{-1}$  were the O–W–O stretching vibrations, and additional peaks of m-WO<sub>3</sub> were also detected, i.e., the O–W–O deformation vibrations at  $326$  and  $272\text{ cm}^{-1}$ , lattice modes at  $186$  and  $133\text{ cm}^{-1}$ . The sharp Raman peaks confirmed the XRD results that m-WO<sub>3</sub> was highly crystalline and ordered.

## Conclusions

The PVP ( $\text{C}_6\text{H}_9\text{NO}_n$ ) and AMT ( $(\text{NH}_4)_6[\text{H}_2\text{W}_{12}\text{O}_{40}] \cdot n\text{H}_2\text{O}$ ) composite nanofibers were prepared by a newly developed electrospinning process from aqueous solutions of PVP and AMT. Our aim was to find the optimal annealing conditions of the PVP/AMT fibers to get high-quality WO<sub>3</sub> nanofibers. We also intended to demonstrate in general the importance of appropriate heating conditions for organic/inorganic electrospun fibers to avoid disintegration of the obtained ceramic nanofibers.

The as-spun PVP/AMT fibers and their annealing were characterized by TG/DTA-MS, XRD, SEM, Raman, and FTIR. The PVP/AMT fibers were  $400$ – $600\text{ nm}$  thick and dozens of micrometer long. According to TG/DTA-MS results, the composite fibers thermally decomposed and oxidized in air in four steps between  $25$  and  $570\text{ }^{\circ}\text{C}$ . Based on these results, the PVP/AMT fibers were annealed in a furnace between  $500$  and  $600\text{ }^{\circ}\text{C}$  and pure m-WO<sub>3</sub> nanofibers were obtained. When  $10\text{ }^{\circ}\text{C min}^{-1}$  heating rate was used at  $600\text{ }^{\circ}\text{C}$ , the WO<sub>3</sub> nanofibers completely

disintegrated. At  $600\text{ }^{\circ}\text{C}$  and with a  $1\text{ }^{\circ}\text{C min}^{-1}$  heating rate, the fibers broke into rods, while at  $500$  and  $550\text{ }^{\circ}\text{C}$  high quality,  $250\text{ nm}$  thick and tens of micrometer long WO<sub>3</sub> nanofibers were obtained. The fibers consisted of  $20$ – $80\text{ nm}$  particles. At  $500\text{ }^{\circ}\text{C}$  the crystalline structure was not ordered enough, therefore  $550\text{ }^{\circ}\text{C}$  and  $1\text{ }^{\circ}\text{C min}^{-1}$  heating rate were found to be the optimal annealing conditions for this set of electrospun nanofibers.

According to the FTIR and Raman spectra, PVP disappeared after annealing at  $550\text{ }^{\circ}\text{C}$ , and based on FTIR only traces of organics were still present. These results confirmed that with optimized heating parameters the organic matter can be effectively removed from the inorganic nanofibers. In harmony with the XRD results, the Raman data also showed that at  $550\text{ }^{\circ}\text{C}$  m-WO<sub>3</sub> was present in highly crystalline and ordered form.

**Acknowledgements** I. M. Sz. thanks for a Marie Curie Intra-European Fellowship (PIEF-GA-2009-235655). The FTIR and Raman studies were supported by the Finnish Centre of Excellence in Computational Molecular Science and the University of Helsinki Research Funds (HENAKOTO).

## References

1. Yang P, Yan R, Fardy M. Semiconductor nanowire: what's next? *Nano Lett.* 2010;10:1529–36.
2. Li JY, Dai H, Li Q, Zhong XH, Ma XF, Meng J, Cao XQ. Lanthanum zirconate nanofibers with high sintering-resistance. *Mater Sci Eng B*. 2006;133:209–12.
3. Ruda HE, Polanyi JC, Yang JSY, Wu Z, Philipose U, Xu T, Yang S, Kavanagh KL, Liu JQ, Yang L, Wang Y, Robbie K, Yang J, Kaminska K, Cooke DG, Hegmann FA, Budz AJ, Haugen HK. Developing 1D nanostructure arrays for future nanophotonics. *Nanoscale Res Lett*. 2006;1:99–119.
4. Choi KJ, Jang HW. One-dimensional oxide nanostructures as gas-sensing materials: review and issues. *Sensors*. 2010;10: 4083–99.
5. Mieszawska AJ, Jalilian R, Sumanasekera GU, Zamborini FP. The synthesis and fabrication of one-dimensional nanoscale heterojunctions. *Small*. 2007;3:722–56.
6. Morales AM, Lieber CM. A laser ablation method for the synthesis of crystalline semiconductor nanowires. *Science*. 1998;279: 208–11.
7. Ye JF, Qi LM. Solution-phase synthesis of one-dimensional semiconductor nanostructures. *J Mater Sci Tech*. 2008;24:529–40.
8. Mozalev A, Khatko V, Bittencourt C, Hassel AW, Gorokh G, Llobet E, Correig X. Nanostructured tungsten oxide semiconductor prepared by anodic and thermal processing of Al/W/Ti thin-film layers. *Chem Mater*. 2008;20:6482–93.
9. Kemell M, Härkönen E, Pore V, Ritala M, Leskelä M. Ta<sub>2</sub>O<sub>5</sub>- and TiO<sub>2</sub>-based nanostructures made by atomic layer deposition. *Nanotechnology*. 2010;21:035301, 8pp.
10. Zhang Z, Shao C, Gao F, Li X, Liu Y. Enhanced ultraviolet emission from highly dispersed ZnO quantum dots embedded in poly(vinyl pyrrolidone) electrospun nanofibers. *J Colloid Interface Sci*. 2010;347:215–20.
11. Sangmanee M, Maensiri S. Nanostructures and magnetic properties of cobalt ferrite (CoFe<sub>2</sub>O<sub>4</sub>) fabricated by electrospinning. *Appl Phys A*. 2009;97:167–77.

12. Nuansing W, Ninnuang S, Jarerboon W, Maensiri S, Seraphin S. Magnesium ferrite ( $MgFe_2O_4$ ) nanostructures fabricated by electrospinning. *Mater Sci Eng B*. 2006;131:147–55.
13. Azad AM, Matthews T, Swary J. Processing and characterization of electrospun  $Y_2O_3$ -stabilized  $ZrO_2$  (YSZ) and  $Gd_2O_3$ -doped  $CeO_2$  (GDC) nanofibers. *Mater Sci Eng B*. 2005;123:252–8.
14. Hou Z, Li C, Yang J, Lian H, Yang P, Chai R, Cheng Z, Lin J. One-dimensional  $CaWO_4$  and  $CaWO_4:Tb^{3+}$  nanowires and nanotubes: electrospinning preparation and luminescent properties. *J Mater Chem*. 2009;19:2737–46.
15. Piperno S, Passacantando M, Santucci S, Lozzi L, La Rosa S.  $WO_3$  nanofibers for gas sensing applications. *J Appl Phys*. 2007;101:124504, 4pp.
16. Shim HS, Kim JW, Sung YE, Kim WB. Electrochromic properties of tungsten oxide nanowires fabricated by electrospinning method. *Sol Energy Mater Sol Cells*. 2009;93:2062–8.
17. Wang G, Ji Y, Huang Y, Yang X, Gouma PI, Dudley M. Fabrication and characterization of polycrystalline  $WO_3$  nanofibers and their application for ammonia sensing. *J Phys Chem B*. 2006;110:23777–82.
18. Ponhan W, Maensiri S. Fabrication and magnetic properties of electrospun copper ferrite ( $CuFe_2O_4$ ) nanofibers. *Solid State Sci*. 2009;11:479–84.
19. Qizheng C, Xiangting D, Jinxian W, Mei L. Direct fabrication of cerium oxide hollow nanofibers by electrospinning. *J Rare Earths*. 2008;26:664–9.
20. Maensiri S, Nuansing W, Klinkaewnarong J, Laokul P, Khemprasisit J. Nanofibers of barium strontium titanate (BST) by sol-gel processing and electrospinning. *J Colloid Interface Sci*. 2006;297:578–83.
21. Lu X, Liu X, Zhang W, Wang C, Wei Y. Large-scale synthesis of tungsten oxide nanofibers by electrospinning. *J Colloid Interface Sci*. 2006;298:996–9.
22. NIST Chemistry Webbook Standard Reference Database, No 69, 01 June. 2005. <http://webbooknistgov/chemistry>.
23. Maensiri S, Laokul P, Promarak V. Synthesis and optical properties of nanocrystalline  $ZnO$  powders by a simple method using zinc acetate and poly(vinyl pyrrolidone). *J Cryst Growth*. 2006;289:102–6.
24. Zhenfeng C, Huijan R, Guixia L, Guangyan G. Synthesis and characterization of terbium-trimesic acid luminescent complex in polyvinylpyrrolidone matrix. *J Rare Earths*. 2006;24:724–7.
25. Li T, Zhong G, Fu R, Yang Y. Synthesis and characterization of Nafion/cross-linked PVP semi-interpenetrating polymer network membrane for direct methanol fuel cell. *J Membr Sci*. 2010;354:189–97.
26. Zhu XF, Lu P, Chen W, Dong J. Studies of UV crosslinked poly(*N*-vinylpyrrolidone) hydrogels by FTIR, Raman and solid-state NMR spectroscopies. *Polymer*. 2010;51:3054–63.
27. Fini A, Cavallari C, Ospitali F. Effect of ultrasound on the compaction of pharmaceuticals and biopharmaceuticals. *Eur J Pharm Biopharm*. 2008;70:409–20.
28. Karavas E, Georgarakis M, Docolis A, Combining BikarisD, EM S. TEM, and micro-Raman techniques to differentiate between the amorphous molecular level dispersions and nanodispersions of a poorly water-soluble drug within a polymer matrix. *Int J Pharm*. 2007;340:76–83.
29. Feldstein MM. Adhesive hydrogels: structure, properties, and applications (a review). *Polym Sci Ser A*. 2004;46:1165–91.
30. Silva MF, da Silva CA, Fogo FC, Pineda EAG, Hechenleitner AAW. Thermal and FTIR study of polyvinylpyrrolidone/lignin blends. *J Therm Anal Calorim*. 2005;79:367–70.
31. Lu F, Liu J, Xu J. Synthesis of chain-like Ru nanoparticle arrays and its catalytic activity for hydrogenation of phenol in aqueous media. *Mater Chem Phys*. 2008;108:369–74.
32. Azhari SJ, Diab MA. Thermal degradation and stability of poly(4-vinylpyridine) homopolymer and copolymers of 4-vinylpyridine with methyl acrylate. *Polym Degrad Stabil*. 1998;60:253–6.
33. Mendes LC, Rodrigues RC, Silva EP. Thermal, structural and morphological assessment of PVP/HA composites. *J Them Anal Calorim*. 2010;101:899–905.
34. Jablonski AE, Lang AJ, Vyazovkin S. Isoconversional kinetics of degradation of polyvinylpyrrolidone used as a matrix for ammonium nitrate stabilization. *Thermochim Acta*. 2008;474:78–80.
35. Sionkowska A, Kozlowska J, Planecka A, Skkopinska-Wisniewska J. Photochemical stability of poly(vinyl pyrrolidone) in the presence of collagen. *J Polym Degrad Stabil*. 2008;93:2127–32.
36. Aggour YA. Copolymerization and characterization of ethylene glycol allenyl methyl ether with *N*-vinyl pyrrolidone. *J Macromol Sci A*. 1998;35:1403–13.
37. Liu C, Xiao C, Liang H. Properties and structure of PVP-lignin “blend films”. *J Appl Polym Sci*. 2005;95:1405–11.
38. Lamasta FR, Nanni F, Camilli L, Matassa R, Carbone M, Gusmano G. Morphology and structure of electrospun  $CoFe_2O_4$ /multi-wall carbon nanotubes composite nanofibers. *Chem Eng J*. 2010;162:430–5.
39. Feng W, Tao H, Liu Y, Liu Y. Structure and optical behavior of nanocomposite hybrid films of well monodispersed  $ZnO$  nanoparticles into poly (vinylpyrrolidone). *J Mater Sci Technol*. 2006;22:230–4.
40. Sivaiah K, Rudremadevi BH, Bubbhudu S, Kumar GB, Varadarajulu A. Structural, thermal and optical properties of  $Cu^{2+}$  and  $Co^{2+}$ : PVP polymer films. *Ind J Pure Appl Phys*. 2010;48:658–62.
41. Jing C, Hou J, Zhang Y, Xu X. Preparation of thick, crack-free germanosilicate glass films by polyvinylpyrrolidone and study of the UV-bleachable absorption band. *J Non Cryst Solids*. 2007;353:4128–36.
42. Jing C, Xu X, Hou J. Preparation of compact  $Al_2O_3$  film on metal for oxidation resistance by polyvinylpyrrolidone. *J Sol Gel Sci Technol*. 2007;43:321–7.
43. Du YK, Yang P, Mou ZG, Hua NP, Jiang L. Thermal decomposition behaviors of PVP coated on platinum nanoparticles. *J Appl Polym Sci*. 2006;99:23–6.
44. Zhang Z, Li X, Wang C, Wei L, Liu Y, Shao C.  $ZnO$  hollow nanofibers: fabrication from facile single capillary electrospinning and applications in gas sensors. *J Phys Chem C*. 2009;113:19397–403.
45. Bogatyrev VM, Borisenko NV, Pokrovskii VA. Thermal degradation of polyvinylpyrrolidone on the surface of pyrogenic silica. *Russ J Appl Chem*. 2001;74:839–44.
46. Mansour SAA, Mohamed MA. Thermal decomposition and the creation of reactive solid surfaces. V. The genesis course of the  $WO_3$  catalyst from its ammonium paratungstate precursor. *Thermochim Acta*. 1988;129:187–96.
47. French GJ, Sale FR. A re-investigation of the thermal decomposition of ammonium paratungstate. *J Mater Sci*. 1981;16:3427–36.
48. Fait MJG, Lunk HJ, Feist M, Schneider M, Dann JN, Frisk TA. Thermal decomposition of ammonium paratungstate tetrahydrate under non-reducing conditions. Characterization by thermal analysis, X-ray diffraction and spectroscopic methods. *Thermochim Acta*. 2008;469:12–22.
49. Lassner E, Schubert WD. Tungsten properties, chemistry, technology of the element, alloys, and chemical compounds. New York: Kluwer Academic/Plenum Publishers; 1999.
50. van Put JW. Crystallisation and processing of ammonium paratungstate (APT). *Int J Refract Met Hard Mater*. 1995;13:61–76.
51. Szilágyi IM, Madarász J, Hange F, Pokol G. On-line evolved gas analyses (EGA by TG-FTIR and TG/DTA-MS) and solid state (FTIR, XRD) studies on thermal decomposition and partial

- reduction of ammonium paratungstate tetrahydrate. Solid State Ion. 2004;172:583–6.
52. Madarász J, Szilágyi IM, Hange F, Pokol G. Comparative evolved gas analyses (TG-FTIR, TG/DTA-MS) and solid state (FTIR, XRD) studies on thermal decomposition of ammonium paratungstate tetrahydrate (APT) in air. *J Anal Appl Pyrol.* 2004;72:197–201.
  53. Szilágyi IM, Madarász J, Hange F, Pokol G. Partial thermal reduction of ammonium paratungstate tetrahydrate. *J Therm Anal Calorim.* 2007;88:139–44.
  54. Szilágyi IM, Hange F, Madarász J, Pokol G. In situ HT-XRD study on the formation of hexagonal ammonium tungsten bronze by partial reduction of ammonium paratungstate tetrahydrate. *Eur J Inorg Chem.* 2006;17:3413–8.
  55. Peters F, Gmelin L, Meyer RJ. Gmelins Handbuch der Anorganischen Chemie. Stickstoff, System Nummer 4. Berlin: Verlag Chemie GmbH; 1936. pp. 645–683.
  56. Szilágyi IM, Madarász J, Király P, Tárkányi G, Tóth AL, Szabó A, Varga-Josepovits K, Pokol G. Stability and controlled composition of hexagonal  $\text{WO}_3$ . *Chem Mater.* 2008;20:4116–25.
  57. Szilágyi IM, Sakó I, Király P, Tárkányi G, Tóth AL, Szabó A, Varga-Josepovits K, Madarász J, Pokol G. Phase transformations of ammonium tungsten bronzes. *J Therm Anal Calorim.* 2009; 98:707–16.
  58. ICDD (International Centre for Diffraction Data) Powder Diffraction File, Release 2008.
  59. Zhang HY, Xu L, Wang EB, Jiang M, Wu AG, Li Z. Photochromic behavior and luminescent properties of novel hybrid organic-inorganic film doped with Preyssler's heteropoly acid  $\text{H}_{12}[\text{EuP}_5\text{W}_{30}\text{O}_{110}]$  and polyvinylpyrrolidone. *Mater Lett.* 2003;57: 1417–22.
  60. Li Y, Li YG, Zhang ZM, Wu Q, Wang EB. A new polyoxotungstate-based  $\text{W}_{72}\text{V}_{30}$  spherical cage. *Inorg Chem Commun.* 2009;12:864–7.
  61. Duplyakin VK, Baklanova ON, Chirkova OA, Antonicheva NV, Arbuzov AB, Voitenko NN, Drozdov VA, Likholobov VA. Interaction of nickel hydroxocarbonate, ammonium paramolybdate, and ammonium metatungstate under mechanical activation. *Kinet Catal.* 2010;51:126–30.
  62. Sunita G, Devassy BM, Vinu A, Sawant DP, Balasubramanian VV, Halligudi SB. Synthesis of biodiesel over zirconia-supported isopoly and heteropoly tungstate catalysts. *Catal Commun.* 2008;9:696–702.
  63. Sarish S, Devassy BM, Böhringer W, Feltcher J, Halligudi SB. Liquid-phase alkylation of phenol with long-chain olefins over  $\text{WO}_3/\text{ZrO}_2$  solid acid catalysts. *J Mol Catal A.* 2005;240:123–31.
  64. Shijun L, Qiyuan C, Oingmin Z, Songqin L. Raman spectral study on isopolytungstates in aqueous solution. *Trans Nonferr Met Soc China.* 1998;8:688–92.
  65. Bukoski RD, Shearin S, Jackson WF, Pamarthi MF. Inhibition of  $\text{Ca}^{2+}$ -induced relaxation by oxidized tungsten wires and paratungstate. *J Pharmacol Exp Ther.* 2001;299:343–50.
  66. Weiner H, Lunk HJ, Friese R, Hartl H. Synthesis, crystal structure, and solution stability of Keggin-type heteropolytungstates  $(\text{NH}_4)_6\text{Ni}_{0.5}^{II}[\alpha\text{-Fe}^{III}\text{O}_4\text{W}_{11}\text{O}_{30}\text{Ni}^{II}\text{O}_5(\text{OH}_2)]\cdot n\text{H}_2\text{O}$ ,  $(\text{NH}_4)_7\text{Zn}_{0.5}^{+}[\alpha\text{-ZnO}_4\text{W}_{11}\text{O}_{30}\text{ZnO}_5(\text{OH}_2)]\cdot n\text{H}_2\text{O}$ , and  $(\text{NH}_4)_7\text{Ni}_{0.5}^{II}[\alpha\text{-ZnO}_4\text{W}_{11}\text{O}_{30}\text{Ni}^{II}\text{O}_5(\text{OH}_2)]\cdot n\text{H}_2\text{O}$  ( $n \approx 18$ ). *Inorg Chem.* 2005;44: 7751–61.
  67. Scheithauer M, Graselli RK, Knözinger H. Genesis and structure of  $\text{WO}_3/\text{ZrO}_2$  solid acid catalysts. *Langmuir.* 1998;14:3019–29.
  68. Faria DLA, Gil HAC, de Queirós AAA. The interaction between polyvinylpyrrolidone and  $\text{I}_2$  as probed by Raman spectroscopy. *J Mol Struct.* 1999;479:93–8.
  69. Daniel MF, Desbat B, Lassegues JC, Gerand B, Figlarz M. Infrared and Raman study of  $\text{WO}_3$  tungsten trioxides, and  $\text{WO}_{3-x}\text{H}_2\text{O}$  tungsten trioxide hydrates. *J Solid State Chem.* 1987; 67:235–47.
  70. Santato C, Odziemkowski M, Ullmann M, Augustynski J. Crystallographically oriented mesoporous  $\text{WO}_3$  films: synthesis, characterization, and applications. *J Am Chem Soc.* 2001;123: 10639–49.
  71. Ramana CV, Utsunomiya S, Ewing RC, Julien CM, Becker U. Structural stability and phase transitions in  $\text{WO}_3$  thin films. *J Phys Chem B.* 2006;110:10430–5.
  72. Siciliano T, Tepore A, Micocci G, Serra A, Manno D, Filippo E.  $\text{WO}_3$  gas sensors prepared by thermal oxidization of tungsten. *Sens Actuator B.* 2008;133:321–6.